https://doi.org/10.5194/egusphere-2025-3776
Preprint. Discussion started: 15 August 2025

The impact of synoptic meteorology on observed surface heat fluxes over the Southern Ocean

Sreenath Avaronthan Veettil[1,2], Tahereh Alinejadtabrizi[1], Steven Siems[1,2], Peter T May[1], Haifeng Zhang[3], and Eric Schulz[3]

[1]School of Earth, Atmosphere and Environment, Monash University, Melbourne, Victoria, Australia
[2]Australian Research Council's Securing Antarctica's Environmental Future (SAEF), Melbourne, Victoria, Australia
[3]Bureau of Meteorology, Melbourne, Victoria, Australia.

Correspondence: Sreenath Avaronthan Veettil (sreenath.av@monash.edu)

Abstract. A 14-year climatology of the bulk sensible and latent heat fluxes (SHF and LHF) made from the Southern Ocean Flux Station (SOFS) is analyzed with respect to the synoptic meteorology and mesoscale cellular convection (MCC). A K-means clustering algorithm identified five synoptic regimes: High Pressure/Ridging (HPR), Tasman Blocking High (TBH), Zonal, Frontal, and Cold Air Advection (CAA). Among these, CAA showed the strongest air-sea coupling, with mean SHF of -40.4 W/m^2 and LHF of -131.0 W/m^2, which are 3.5 and 2 times greater than the overall mean, respectively. This striking increase in fluxes during CAA is associated with a high marine cold-air outbreak index (M-index) and weak inversion coupled with cold and dry air transport towards SOFS by the strong south-westerly wind. The SOFS measurements are also employed to evaluate ERA5 fluxes, finding that ERA5 accurately represents the observed bulk SHF and LHF, with a mean bias of 1.6 W/m^2 for SHF and -6.2 W/m^2 for LHF, along with significant correlation coefficients of r=0.9 and 0.92, respectively. Turning to open and closed MCC, relatively weak differences in the fluxes are observed between these two states, suggesting that the SHF and LHF are not the primary drivers in the transition between open and closed MCC. In open MCC, SHF and LHF show a strong correlation with the M-index, while closed MCC is associated with a stable atmosphere with a strong inversion, where the M-index relationship with surface fluxes is weak.

1 Introduction

The Southern Ocean (SO) is responsible for about 75±22% of the excess heat absorbed by the world's oceans each year, moderating global temperatures (Frolicher et al., 2015; Williams et al., 2024). Sea surface temperature (SST) variability and heat uptake into the SO profoundly impact climate change and global circulation, which may substantially influence remote tropical climate systems in the coming decades (Jeong et al., 2025). Although the SO influences the global climate, many climate models have consistently shown a notable radiative bias over the SO for several generations (Schuddeboom and McDonald, 2021). The radiative bias in the Coupled Model Intercomparison Project (CMIP) phase 5 over the SO has been attributed to errors in depicting cloud fraction and phase (McFarquhar et al., 2021) and resulting substantial warm biases in SO SST (Sallée et al., 2013; Meijers, 2014).

https://doi.org/10.5194/egusphere-2025-3776
Preprint. Discussion started: 15 August 2025

Understanding the climate system over the SO requires continuous monitoring of heat exchange between the ocean and the atmosphere. While many advances have been made in assessing surface fluxes, achieving closure of energy and water budgets at the air-sea interface over the SO remains a challenge, primarily due to limited direct measurements (Bharti et al., 2019). The Ocean Reanalysis Intercomparison Project (ORA-IP) ensemble, which includes 16 flux estimates, shows a global average positive bias in net heat gain of 4.2 ± 1.1 W/m^2 from 1993 to 2009. The variability among these products increases significantly in the SO, while it remains relatively stable in the northern subtropical and higher latitudes (Valdivieso et al., 2017). ERA5, the most recent global reanalysis output from the European Centre for Medium-Range Weather Forecasts (ECMWF), has been used widely in weather and climate research, which uses data simulation systems based on coupled numerical models to assimilate multiple fields gathered from surface observations and remote sensing techniques (Dee et al., 2011). Reanalysis data suffer from various sources of uncertainty, including observation errors, heterogeneity of data sources in space and time, and uncertainty in the numerical model, such as the impact of finite resolution and uncertainties in parameterizations (Bosilovich et al., 2008; Liu et al., 2011), so their performance over the SO requires evaluation. In line with this, significant mean state differences of surface net heat flux of up to 50 W/m^2 were observed between reanalysis products such as ERA5, JRA-55, and NCEP-II over vast swaths of the SO (Swart et al., 2019). Hyder et al. (2018) combined Atmospheric and Coupled Model Intercomparison Project (AMIP5/CMIP5) simulations with observations and equilibrium heat budget theory and demonstrated that within the CMIP5 ensemble, variations in SST biases in the SO are mainly driven by net surface flux bias variations in AMIP5 atmospheric models. The international climate research community aims to precisely measure each element of the surface heat budget within a 5 W/m^2 range, with a spatial resolution of 1° and a temporal resolution of 3–6 hours (Curry et al., 2004). To reach this objective, it is necessary to establish an adequate number of direct flux measurement stations in remote areas such as the SO. The Southern Ocean Flux Station (SOFS), located at 47°S, 142°E, was established under the auspices of the Australian Integrated Marine Observing System (IMOS) (Hill et al., 2010; Schulz et al., 2012), is regarded as the benchmark for the measurement of flux data over the high latitudes of the SO, and the measurements made by the maintained surface moorings have proven to be of high value (Josey et al., 2023).

Across the SO, an increase in the flux from the ocean to the atmosphere can intensify extratropical storms (Yau and Jean, 1989; Kuwano-Yoshida and Minobe, 2017) and alter the stability of both the ocean and atmosphere (Neiman et al., 1990; Chen et al., 2010). Surface heat fluxes play a vital role in cyclogenesis (Yokoyama and Yamamoto, 2019), but the stage of cyclonic development may also affect flux variability. Earlier research has indicated a potential link between mesoscale SST anomalies and synoptic storms (Small et al., 2008; Su et al., 2018), feeding back on the air-sea fluxes. Bharti et al. (2019) (Bharti et al., 2019) observed a notable decrease in heat fluxes within the warm sector of storms over the SO, with significant variations in sensible heat flux (SHF) ranging from -91 to 103 W/m^2 and latent heat flux (LHF) from -105 to 180 W/m^2. The greatest variability in air-sea flux magnitude over the SO occurs during winter, marked by synoptic-scale cold air outbreaks, where cold, dry air moves over warmer water, leading to episodic high flux events (Shaman et al., 2010). Despite these findings, there remains a notable gap in the literature regarding the influence of different synoptic regimes on air-sea interactions over the SO, particularly based on long-term observational data.

https://doi.org/10.5194/egusphere-2025-3776
Preprint. Discussion started: 15 August 2025

At 47 °S, the synoptic meteorology of the SOFS station is primarily defined by the nearby SO storm track (Truong et al., 2020) with the rapidly evolving weather patterns defining the structure of the marine atmospheric boundary layer (MABL) clouds (McCoy et al., 2017; Naud et al., 2016). Wood and Hartmann (2006) categorized four basic structures for MABL clouds: open mesoscale cellular convection (MCC), closed MCC, no MCC, and disorganized cellular clouds. Lang et al. (2024) showed that the location and frequency of open and closed MCC clouds are closely related to sea surface temperature (SST) gradients, suggesting that the turbulent fluxes may help govern the structure of this cloud, as has been noted over the subtropics (Eastman et al., 2022). The role of atmospheric stability and inversion indices in modulating air-sea coupling during open and closed MCC occurrence is still not well understood. Additionally, there has been no validation of ERA5 flux data during open and closed MCC periods, which is crucial for understanding how boundary layer clouds affect the surface energy budget.

Using 14 years of observations from the SOFS, the present study examines air-sea interaction, i.e., the SHF and LHF, over the SO as defined by the ERA5-based synoptic meteorology. Across the different synoptic regimes, we analyze these fluxes and their relationship with the thermodynamic structure of the MABL, as defined by the cold air outbreak index (M index) and the estimated inversion strength (EIS). By focusing on open and closed MCC periods, we examine the air-sea interaction and the importance of entrainment-driven moisture transport in regulating the water budget. Given that the SOFS observations are currently not assimilated into reanalysis products, we further employ the observations to evaluate the ERA5 fluxes seasonally, across the synoptic regimes and MCC cloud structure at SOFS.

2 Data and methods

2.1 SOFS measurement

This study utilizes data from the SOFS south of Tasmania (47°S, 142°E) and spans from March 2010 to May 2023. Measurements are collected at a 1-minute sample rate and then averaged to 1-hour means to align with the temporal resolution of the ERA5 data used in this study. The surface variables selected from SOFS measurements for this research include: air temperature (AT, 2m), mean sea-level pressure (MSLP), relative humidity (RH, 2m), wind speed (10m), sea surface temperature (SST).

It is important to note that this research incorporates only 62% of the hourly data for the above period, with the remaining part excluded due to the missing observations from the buoy (see Fig. S1 in the Supplement). The SHF and LHF were determined using the bulk algorithm from the Coupled Ocean-Atmosphere Response Experiment (COARE, version 3.5), as described by Fairall et al. (1996) and Edson et al. (2013). The algorithm incorporates near-surface meteorological data, ocean observations, and radiative elements. These COARE 3.5 bulk fluxes derived from SOFS measurements are used as in situ observations to validate ERA5 flux in this research. Following ERA5, the upward flux (from the ocean to the atmosphere) is represented as negative.

https://doi.org/10.5194/egusphere-2025-3776
Preprint. Discussion started: 15 August 2025

All bulk parameterization algorithms utilize the Monin–Obukhov similarity theory (MOST) (Monin and Obukhov, 1954), which is expressed by the following equation:

$$\mathrm{SHF} = \rho \cdot C_p \cdot C_H \cdot U \cdot (\mathrm{SST} - \mathrm{AT}) \tag{1}$$

where: ρ = Air density (kg/m^3), Cp = Specific heat capacity of air (J/kg·K), CH = Sensible heat transfer coefficient, U = Wind speed at reference height (m/s), SST = Sea surface temperature (K or °C), AT = Air temperature at reference height (K or °C).

$$\mathrm{LHF} = \rho \cdot L_v \cdot C_E \cdot U \cdot (q_s - q_a) \tag{2}$$

where: ρ = Air density (kg/m^3), Lv = Latent heat of vaporization (J/kg), CE = Latent heat transfer coefficient (dimensionless), U = Wind speed at reference height (m/s), qs = Specific humidity at the surface (kg/kg), qa = Specific humidity at reference height (kg/kg).

2.2 Synoptic classification using K-mean clustering on ERA5 data

The K-Mean is one of the simplest and non-hierarchical clustering techniques based on vector quantization developed by Hartigan and Wong (1979). The technique requires two inputs: (1) the number of clusters (k) and (2) the initial random positions of each cluster's centroids. Each measurement is assigned to its nearest centroid, and the centroids are then updated iteratively based on the cluster's values. To minimize the sum of squared deviations inside clusters, the operation is repeated until the centroid positions settle. For this study, ERA5 hourly data from 2010 to 2023 is employed to perform K-means clustering of weather types at the SOFS location. Following Lang et al. (2018), the K-mean incorporates four variables (temperature, RH, zonal wind, and meridional wind) at three levels (925, 850, and 700 hPa), along with three surface variables (pressure, air temperature, and RH). Before clustering, each variable is normalized (resulting in zero mean and unit standard deviation).

2.3 Calculating inversion strength and M-index

The EIS Wood and Hartmann (2006) is defined as:

$$\mathrm{EIS} = \mathrm{LTS} - \Gamma_m \left(Z_{700} - Z_{\mathrm{LCL}}\right) \tag{3}$$

In this equation, LTS represents Lower Tropospheric Stability ($\theta_{700} - \theta_0$), θ and Z denote potential temperature and geopotential height, respectively. The subscripts "700", "0", and "LCL" correspond to the 700 hPa level, 1000 hPa level, and Lifting Condensation Level (LCL), respectively. Γ_m signifies the moist adiabatic θ gradient at 850 hPa, calculated using the average temperature between the 1000 and 700 hPa levels. The M-index (Kolstad and Bracegirdle, 2008) evaluates boundary layer stability and is an important indicator of cloud formation characteristics in high-latitude regions. M is defined as the difference between the surface skin and the 850 hPa potential temperature.

https://doi.org/10.5194/egusphere-2025-3776
Preprint. Discussion started: 15 August 2025

2.4 Himawari-8 data

This research uses Advanced Himawari Imager (AHI) data from the Himawari-8 geostationary meteorological satellite (Bessho et al., 2016) to categorize open and closed MCC. The AHI provides spatial and temporal resolutions of 1–5 km and 10 min, respectively. A Convolutional Neural Network (CNN) model was developed using the TensorFlow Python package to classify open and closed MCC from Himawari-8 satellite imagery (Lang et al., 2022). The model was trained utilizing hourly brightness temperature data with 5 km resolution from channel 11, which operates at a wavelength of 8.6 μm and subsequently applied for MCC classification from 2016 to 2021. We used the 2.5°×2.5° box at SOFS to identify the open and closed MCC, and the occurrence of open/closed MCC is defined when 80% of the box is covered by open/closed cells.

2.5 HYSPLIT model data

The 72-hour back-trajectories were computed at an altitude of 500 meters above SOFS using the Hybrid Single-Particle Lagrangian Integrated Trajectory (HYSPLIT) model (Draxler and Hess, 1998) to investigate the origins of air masses during different synoptic conditions. Hourly data from ERA5 served as the input for the meteorological parameters utilized in the back trajectory modeling.

3 Results

3.1 Characteristics of synoptic types and air-sea interaction over the SO

Located roughly midway between the SO storm track and Tasmania, the meteorology of the SOFS site (marked with a star in Fig. 1a) is primarily defined by the progression of mid-latitude cyclones along the SO storm track, although the frontal systems are slightly suppressed during the summer when the subtropical ridge moves to higher latitudes (Alinejadtabrizi et al., 2025). K-means clustering of meteorological variables at SOFS identifies five synoptic weather regimes that align with the first five clusters found in Truong et al. (2020). We now discuss the dynamic and thermodynamic features of these weather regimes, as well as the characteristics of air-sea interactions at the SOFS.

High Pressure/Ridging (HPR), frequency of occurrence 22.9%: The HPR is associated with weak northwesterly low-level wind (Fig. 1a) and exhibits no discernible seasonality over the SOFS (Fig. 2a). HPR is an extension of the high-pressure belt over southern Australia with stable conditions resulting in weak precipitation rates in ERA-5 of 0-0.025 mm/hr. However, a significant amount of rainfall is seen southwest of SOFS during this weather regime. The HPR regime has a strong inversion layer with dry and warm air in the free troposphere (Fig. 1f). The temperature inversion begins at 900 hPa, and the temperature-dewpoint profile indicates the elevated LCL for a surface parcel at 937 hPa.

Tasman Blocking High (TBH), frequency of occurrence 12.0%: The TBH reflects a blocking anticyclone over the Tasman Sea Risbey et al. (2009). It demonstrates a pronounced seasonal cycle, with a maximum frequency during the summer (Fig. 2a). As SOFS is relatively far from the blocking high over the Tasman Sea, the wind profile shows moderate intensity with a consistent northwesterly direction (Fig. 1b). Similar to HPR, the ERA5 surface precipitation rate is weak during TBH con-

https://doi.org/10.5194/egusphere-2025-3776
Preprint. Discussion started: 15 August 2025

ditions, and the centre of the surplus rainfall is located southwest of SOFS. Thermodynamic profile Fig. 1g highlights that the composite inversion is stronger than the HPR from 950 hPa during TBH, and a dew point depression exceeding 15 °C is observed at 700 hPa. However, the thermodynamic profile at the surface level suggests a moist and warm lower atmosphere and the mean LCL for this weather regime is noted at 966 hPa.

Zonal, frequency of occurrence 26.6%: The zonal is the most frequent synoptic weather regime over SOFS and exhibits no seasonality. The composite zonal pattern depicts a widespread subtropical ridge south of Australia with lower-level westerly winds at SOFS (Fig. 1c). Similarly, the SkewT-LogP diagram highlights a moderate temperature inversion in the mid-troposphere for this weather regime. The trajectories in Fig. 1m indicate that the predominant source of air masses associated with this regime originates from the west of the SOFS.

Frontal, frequency of occurrence 15.5%: The frontal cluster exhibits a weak seasonal cycle, slightly peaking during winter (Fig. 2a). This regime features strong north-westerly winds intensified by a low-pressure trough south of SOFS. It includes the warm conveyor belt of the mid-latitude cyclones along the storm track (Fig. 1d, n). Frontal soundings display a deep layer of near-saturated air from 1000 to 500 hPa with LCL at 965 hPa, triggering the most intense rainfall at SOFS. Specifically, the ERA5 indicates a rain rate of 0.35-0.40 mm/hr during the frontal passage through SOFS.

Cold Air Advection (CAA), frequency of occurrence 22.6%: The CAA is the dominant wintertime synoptic regime, with a frequency of approximately 30% in August. The maximum CAA frequency in winter is associated with a northward shift of the subtropical ridge and associated intrusion of cold airmass from the far south of SOFSS (Hoskins and Hodges, 2019). This weather regime is related to post-frontal conditions, with the high-pressure centre located northwest of the SOFS (Fig. 1e). During CAA, the SOFS encounters the south-westerly winds of a pristine SO airmass (Fig. 1e, o), associated with cold air outbreaks. The surface is extremely dry, with a dewpoint depression of nearly 8 °C and the mean LCL extending to 912 hPa.

We now examine the characteristics of air-sea interaction at SOFS. At SOFS, the mean value of SHF is -11.6 W/m^2 and LHF is -67.5 W/m^2, with LHF being 5.8 times stronger than SHF (Table 1). Observational data and ERA5 analyses show that the SHF and LHF significantly increase between May and September (late autumn to early spring) (Fig. 2b, c). Although SST and air temperature at 2m (AT) reach their lowest between May and September, their difference is greatest during this period, approaching nearly 1°C (Fig. 2d, e). This strong SST-AT gradient, combined with strong 10-m wind speeds of 11-11.5 m/s, produces a maximum of the SHF (Fig. 2g). Concurrently, the dry near-surface conditions, with a mean 2m specific humidity (qa) of 5.5 g/kg and a maximum 10-meter wind speed, enhance the LHF between late autumn and early spring.

3.2 Changes in air-sea interactions associated with synoptic types over SO

Air-sea fluxes, including the SHF and LHF, are key variables related to the coupling between the ocean and the atmosphere. Figure 3 shows that the air-sea interaction process varies significantly between synoptic types, and CAA is associated with the most intense SHF and LHF. During CAA events, the mean SHF and LHF released from the ocean were -40.4 W/m^2 and -131.1 W/m^2, respectively, approximately 3.5 and 2 times stronger than the overall average (Fig. 3a and b; Table 1). The intense, cold, and dry southerly winds associated with CAA cause a sharp decrease in AT (Fig. 4), which creates favourable conditions for significant heat and moisture uptake from the ocean surface. The two-dimensional histogram analysis in Fig. 5 reveals that

https://doi.org/10.5194/egusphere-2025-3776
Preprint. Discussion started: 15 August 2025

intense SHF and LHF during CAA are associated with a higher M index and lower EIS, where the M-index shows a maximum density between -4 and 4 K. Importantly, CAA exhibits the highest M index (mean -1.7 K) and the lowest EIS (mean 1.8 K), indicating increased instability and a weaker temperature inversion than the other weather regimes at SOFS (Fig. 5e).

The mean SHF and LHF for HPR are -11.6 W/m^2 and -56.8 W/m^2, and the weak fluxes result from the weak surface winds shown in Fig. 4d. The HPR represents a highly stable atmosphere with a mean M-index of -8.0 K and EIS of 6.2 K, and there is no solid relationship between these surface fluxes and the M index. For the TBH and frontal clusters, the mean SHF transfers from the atmosphere to the ocean (Fig. 3a, Table 1), which is related to warm air advection from the northwest sector of SOFS, as shown by the increase in SST and AT in Fig. 4a and b. Additionally, TBH and frontal clusters correspond to minimal LHF exchange from the ocean, reflecting a relatively moist surface level (Fig. 4c). It is noteworthy that, at SOFS, the combined surface fluxes (LHF + SHF) are lowest (-18 W/m^2) during these periods of warm air advection. The M-index and EIS are skewed toward more negative and positive extremes in the TBH regime, respectively, with a mean value of -12.9 K for the M-index and 7 K for the EIS. Similar to the HPR regime, no significant relationship exists between the M-index and surface fluxes in TBH, as illustrated in Fig. 5b and g. However, in the frontal regime, surface fluxes increase with the M-index, and it has mean values of -8.6 K for the M-index and 2.0 K for EIS. The SHF distribution in the zonal cluster shows that the heat exchange between the ocean and the atmosphere is generally in equilibrium, indicating a weak thermal gradient between the sea surface and the overlying air (Fig. 4a and b). In this regime, the M-index is densely distributed between -10 K and -5 K, and surface fluxes increase significantly with the M-index.

The changes observed in SHF, LHF and their drivers during the weather regimes at the SOFS were examined in a case study from February 11 to February 15, 2019, to represent how the transition between synoptic regimes occurs at SOFS and the associated changes in air-sea interaction (Fig. 6). It is evident that when transitioning from a frontal regime to CAA, there is a sharp increase in both SHF and LHF exchanges, a noticeable decrease in mean sea-level pressure (MSLP), and an increase in surface wind speed (Fig. 6a, b). After the passage of this synoptic system, zonal weather regimes emerge, resulting in a significant weakening of air-sea interactions. Other surface parameters, such as AT, qa, and stability indicators such as the M-index and EIS, also closely mirror the patterns observed in Fig. 4 and 5 for all synoptic regimes noted at SOFS.

3.3 Validation of ERA5 fluxes with SOFS measurements

Comparing the mean observed fluxes with ERA5 at the nearest grid point shows that ERA5 underestimates the observed SHF by 1.7 W/m^2 and overestimates the LHF by -6.2 W/m^2 (Fig. 3 and Table 2). The underestimation of SHF can be attributed to a negative bias in SST, AT, and 10 m wind speed in ERA5 (Fig. 4). However, the dry bias in qa creates a high humidity gradient between the ocean surface and the 2 m level, which overcomes the negative bias in wind speed and overestimates LHF in ERA5. The bias in SHF and LHF varies with the season (Fig. 2b and c), with the maximum bias in SHF observed during the austral winter (June-August) when the bias in surface wind speed peaks. In summer (December to February), ERA5 SHF accurately represents the magnitude of the observed SHF; in contrast, the biases in LHF vary significantly from month to month. Overall, ERA5 shows significant skill in accurately representing the variations of SOFS flux, as evidenced by solid correlation coefficients of r=0.90 ($p<0.01$) for SHF and 0.92 ($p<0.01$) for LHF.

https://doi.org/10.5194/egusphere-2025-3776
Preprint. Discussion started: 15 August 2025

Examining the performance of ERA5 fluxes for individual weather regimes, it is evident that there is a significant overestimation of the SHF and LHF during CAA events, with average biases of -2.9 W/m^2 for SHF and -12.1 W/m^2 for LHF, as shown in Table 2. The pronounced overestimation of ERA5 SHF during CAA is attributed to a greater mean SST-AT difference, recorded at 2.4 °C, in contrast to the observed SST-AT difference of 2 °C. Similarly, the overestimation of ERA5 LHF for CAA is influenced by a drier surface level, with a mean qa of 4.5 g/kg in ERA5, compared to the observed value of 4.9 g/kg. Despite this overestimation, ERA5 fluxes demonstrate strong correlations with observed values of fluxes: r = 0.88 ($p < 0.01$) for SHF and r = 0.87 ($p < 0.01$) for LHF. For the TBH and frontal clusters, ERA5 overestimates the SHF from the atmosphere to the ocean (Fig. 3), with a mean bias of 3.3 W/m^2 and 6.4 W/m^2, respectively. ERA5 LHF has a mean bias of -0.05 W/m^2 for the TBH regime, the lowest bias among all synoptic regimes, followed by the frontal regime, with a mean LHF bias of -2.2 W/m^2. The most frequently observed zonal clusters reveal a mean SHF bias of 1.6 W/m^2 and an LHF bias of -8.2 W/m^2, with correlation coefficients of r = 0.80 ($p < 0.01$) for SHF and r = 0.87 ($p < 0.01$) for LHF (Table 2). In summary, the ERA5 shows significant skill in reproducing observed fluxes, overall and across the synoptic regimes.

3.4 Influence of synoptic types on MCC and differences in air-sea interaction for open and closed MCC

The frequency of open and closed MCCs associated with synoptic types over the SO highlights that open MCCs are more prevalent during the CAA regime (Fig. 7a), while closed MCCs are most frequent in high-pressure weather regimes due to strong lower tropospheric inversions (McCoy et al., 2017; Lang et al., 2022). Frontal systems increase atmospheric instability, making boundary layer clouds, like open and closed MCCs, less common. Open MCC has a mean of -31.6 W/m^2 for SHF and -130.5 W/m^2 for LHF, and closed MCC has a mean of -26.3 W/m^2 for SHF and -102.8 W/m^2 for LHF (Table 1). Hence, the difference in the SHF and LHF between these boundary layer clouds is moderate, likely due to comparable SST, AT, and qa for these two states (Fig. 4). However, the 10 m wind speed exhibits a considerable difference, with increased wind speed observed in open MCC. This increased wind speed is likely the primary driver of moderately higher surface fluxes in open MCC.

Open MCC clouds are characterized by an M index/EIS range of -5 to 5 K; and in these conditions the SHF and LHF demonstrate a significant increase as the M index increases under weak EIS (Fig. 8). In contrast, closed MCC occur under a more stable atmosphere with M index ranging from -15 to -5 K and an EIS range of 5 to 15 K (McCoy et al., 2017). Under closed MCC, SHF and LHF exchanges also increase with the M index; however, at a considerably slower rate than in open MCC (Fig. 8). The evaluation of ERA5 flux performance against observational data during open and closed MCC periods is presented in Table 2. For open MCCs, the correlation coefficients are high, measuring 0.89 and 0.88 for both SHF and LHF, respectively. The mean biases in ERA5 fluxes correspond to values of -4.9 W/m^2 for SHF and -8.9 W/m^2 for LHF. In closed MCC, the ERA5 SHF shows a minimal bias of 0.8 W/m^2 and a strong correlation coefficient of 0.92, while the ERA5 LHF has the highest correlation of 0.94 with observations, accompanied by a bias of -7.7 W/m^2. These results underscore that ERA5 fluxes effectively represent SHF and LHF from observations under both open and closed MCC over the SOFS, with slightly better performance observed for closed MCC episodes.

https://doi.org/10.5194/egusphere-2025-3776
Preprint. Discussion started: 15 August 2025

4 Discussion and conclusion

We identified five weather regimes over the SOFS buoy's site: HPR, TBH, Zonal, Frontal, and CAA. The different synoptic regimes significantly impact the modulation of SHF and LHF over the SO (Fig. 3). Notably, the CAA episodes are associated with intense SHF and LHF release from the ocean, tied to the influx of dry and cold air from the high latitudes south of SOFS. The TBH cluster is characterized by relatively small air-sea interaction, indicative of warm and moist air advection from the northwestern sector of the SOFS. The CAA, zonal, and frontal weather regimes have weak inversion strength and are associated with an increased exchange of SHF and LHF with the M-index (Fig. 5). In contrast, the atmosphere has a strong inversion layer in the HPR and TBH regimes, where the relationship between the M-index and SHF/LHF is not evident. Our findings suggest that bulk surface fluxes from ERA5 exhibit significant skill in reproducing the SOFS bulk fluxes with an overall correlation of 0.90 ($p<0.01$) for SHF and 0.92 for LHF ($p<0.01$). Given the primary role that MABL clouds play in the Earth's radiation budget, it has long been a priority to understand the mechanisms that govern the transition of cloud morphology from one state to another. In the subtropics, increases in SHF and LHF have been identified as critical factors in the transition from stratocumulus to trade cumulus clouds (Wyant et al., 1997; Sandu and Stevens, 2011) along a Lagrangian trajectory. However, our findings indicate that open MCCs are associated with a mean SHF of -31.6 W/m^2 and LHF of -130.5 W/m^2, while closed MCCs are associated with a mean SHF of -26.4 W/m^2 and LHF of -102.8 W/m^2 (Fig. 3, Table 1). Therefore, the transition from closed to open MCC states exhibits relatively small variations in SHF and LHF (1.2% and 1.3% for SHF and LHF, respectively), suggesting a more limited role for these fluxes over the SO in the transition of these MABL clouds. From the Eulerian perspective of the SOFS, SST and AT undergo only weak variations between cloud morphological states (Fig. 4a and b), but the surface-level wind speed (Fig. 4d) and MSLP (see Fig. S2) show considerable differences for these two cloud states, indicating that synoptic meteorology may be the primary driver behind the transition.

The LHF are of further importance in constraining the water budget over the SO, given that a precipitation rate of 1 mm/day is balanced by the evaporation from an LHF of ~28.9 W/m^2 over the cold waters of the SO. Currently, there are significant discrepancies in the intensity and spatial distribution of precipitation products across the SO (Manton et al., 2020; Boisvert et al., 2020; Behrangi and Song, 2020; Montoya Duque et al., 2023), mainly due to the scarcity of high-quality observations in this remote and harsh environment (Siems et al., 2022). A study by Alinejadtabrizi et al. (2024) at the Kennaook/Cape Grim observatory (~620 km northeast of SOFS) reported that the average precipitation rate (P) of open MCCs is 1.7 mm/day. In contrast, closed MCCs exhibited a rate of 0.3 mm/day. However, at SOFS, ERA5 indicates a precipitation rate of 1.6 mm/day for open MCC and 0.7 mm/day for closed MCC. Applying the ERA5 precipitation rates with the SOFS fluxes reveals a disparity between evaporation (E) and precipitation in open and closed MCCs over the SO. Specifically, for closed MCCs, the evaporation equivalent of the LHF, E, is 3.4 mm/day, resulting in E – P = 3.4 - 0.7 = 2.7 mm/day. This indicates that water is being added to the MABL during periods of closed MCC. Assuming that specific humidity remains steady over time, the entrainment of dry, overlying air is necessary to maintain equilibrium in the MABL-specific humidity. In the case of open MCC, E - P = 4.2 - 1.6 = 2.6 mm/day, it also adds significant water to the MABL, necessitating the transport of dry air from the free troposphere. The closed MCC is characterized by a strong inversion at approximately 900 hPa (Fig. 7c) and the inversion

https://doi.org/10.5194/egusphere-2025-3776
Preprint. Discussion started: 15 August 2025

for open MCC is weaker and occurs at a higher altitude (~820 hPa), allowing for the formation of deeper convective clouds. The entrainment rate (we), calculated using the approximation we = E-P/qft-qsfc, is 4.3 cm/s for closed MCC, which is much larger than the entrainment rate in open MCC, i.e., 1.6 cm/s (qft is the specific humidity in the free troposphere and qsfc is the specific humidity at the surface from ERA5). The steeper moisture gradient between the surface and the lower free troposphere results in reduced entrainment in open MCC, whereas the weaker moisture gradient in closed MCC leads to a more intense entrainment rate than in open MCC. Consistent with our findings, Berner et al. (2011, 2013) used numerical simulations to find that entrainment is weaker in pockets of open cells due to reduced turbulence at the cloud top compared to the surrounding overcast stratocumulus field. This difference in the entrainment rate between open and closed MCC has a direct impact on both the macrophysical and microphysical properties of the clouds, highlighting the importance of synoptic meteorology in governing cloud properties across the SO.

Code availability. Codes are available upon reasonable request to the corresponding author. The COARE 3.5 model code can be downloaded from https://github.com/NOAA-PSL/COARE-algorithm.

Data availability. The SOFS measurements can be accessed through the Australian Ocean Data Network (AODN) Portal at https://thredds.aodn.org.au/thredds/catalog.html. The ERA5 data is available at https://cds.climate.copernicus.eu. The open and closed MCC data can be obtained from Francisco Lang upon reasonable request.

Author contributions. S.A.V. and S.S. designed the study. S.A.V performed the analysis, and wrote the initial manuscript. S.S. and P.M. were actively involved in constructive discussions of the results, providing valuable ideas and feedback. T.A. carried out the trajectory analysis using HYSPLIT. H.Z. and E.C. helped in acquiring SOFS data. All authors contributed to the final version of the manuscript.

Competing interests. The authors declare that they have no known competing financial interests or personal relationships that could have influenced the work reported in this paper.

Acknowledgements. This research has been supported by the Australian Research Council's Securing Antarctica's Environmental Future (SAEF) Project (SRI200100005). The SOFS data were sourced from Australia's Integrated Marine Observing System (IMOS)-IMOS is enabled by the National Collaborative Research Infrastructure Strategy (NCRIS). S.A.V. is thankful to Francisco Lang for providing open and closed MCC data for this research.

https://doi.org/10.5194/egusphere-2025-3776
Preprint. Discussion started: 15 August 2025

References

Alinejadtabrizi, T., Lang, F., Huang, Y., Ackermann, L., Keywood, M., Ayers, G., Krummel, P., Humphries, R., Williams, A. G., Siems, S. T., et al.: Wet deposition in shallow convection over the Southern Ocean, npj Climate and Atmospheric Science, 7, 76, https://doi.org/10.1038/s41612-024-00625-1, 2024.

Alinejadtabrizi, T., Huang, Y., Lang, F., Siems, S., Manton, M., Ackermann, L., Keywood, M., Humphries, R., Krummel, P., Williams, A., et al.: Contributions of the synoptic meteorology to the seasonal cloud condensation nuclei cycle over the Southern Ocean, Atmospheric Chemistry and Physics, 25, 2631–2648, https://doi.org/10.5194/acp-25-2631-2025, 2025.

Behrangi, A. and Song, Y.: A new estimate for oceanic precipitation amount and distribution using complementary precipitation observations from space and comparison with GPCP, Environmental Research Letters, 15, 124 042, https://doi.org/10.1088/1748-9326/abc6d1, 2020.

Berner, A., Bretherton, C., and Wood, R.: Large-eddy simulation of mesoscale dynamics and entrainment around a pocket of open cells observed in VOCALS-REx RF06, Atmospheric Chemistry and Physics, 11, 10 525–10 540, https://doi.org/10.5194/acp-11-10525-2011, 2011.

Berner, A., Bretherton, C., Wood, R., and Muhlbauer, A.: Marine boundary layer cloud regimes and POC formation in a CRM coupled to a bulk aerosol scheme, Atmospheric Chemistry and Physics, 13, 12 549–12 572, https://doi.org/10.5194/acp-13-12549-2013, 2013.

Bessho, K., Date, K., Hayashi, M., Ikeda, A., Imai, T., Inoue, H., Kumagai, Y., Miyakawa, T., Murata, H., Ohno, T., et al.: An Introduction to Himawari-8/9—Japan's New-Generation Geostationary Meteorological Satellites, Journal of the Meteorological Society of Japan. Ser. II, 94, 151–183, https://doi.org/10.2151/jmsj.2016-009, 2016.

Bharti, V., Fairall, C., Blomquist, B., Huang, Y., Protat, A., Sullivan, P., Siems, S., and Manton, M.: Air-sea heat and momentum fluxes in the Southern Ocean, Journal of Geophysical Research: Atmospheres, 124, 12 426–12 443, https://doi.org/10.1029/2018JD029761, 2019.

Boisvert, L. N., Webster, M. A., Petty, A. A., Markus, T., Cullather, R. I., and Bromwich, D. H.: Intercomparison of precipitation estimates over the Southern Ocean from atmospheric reanalyses, Journal of Climate, 33, 10 627–10 651, https://doi.org/10.1175/JCLI-D-20-0044.1, 2020.

Bosilovich, M. G., Chen, J., Robertson, F. R., and Adler, R. F.: Evaluation of global precipitation in reanalyses, Journal of Applied Meteorology and Climatology, 47, 2279–2299, https://doi.org/10.1175/2008JAMC1921.1, 2008.

Chen, S., Campbell, T. J., Jin, H., Gaberšek, S., Hodur, R. M., and Martin, P.: Effect of two-way air–sea coupling in high and low wind speed regimes, Monthly Weather Review, 138, 3579–3602, https://doi.org/https://doi.org/10.1175/2009MWR3119.1, 2010.

Curry, J. A., Bentamy, A., Bourassa, M. A., Bourras, D., Bradley, E. F., Brunke, M. A., Castro, S., Chou, S.-H., Clayson, C. A., Emery, W. J., et al.: Seaflux, Bulletin of the American Meteorological Society, 85, 409–424, https://doi.org/10.1175/BAMS-85-3-409, 2004.

Dee, D., Uppala, S. M., Simmons, A. J., Berrisford, P., Poli, P., Kobayashi, S., Andrae, U., Balmaseda, M., Balsamo, G., Bauer, P., et al.: The ERA-Interim reanalysis: Configuration and performance of the data assimilation system, Quarterly Journal of the Royal Meteorological Society, 137, 553–597, https://doi.org/10.1002/qj.828, 2011.

Draxler, R. R. and Hess, G. D.: An overview of the HYSPLIT_4 modelling system for trajectories, Australian Meteorological Magazine, 47, 295–308, https://www.researchgate.net/profile/G-Hess/publication/239061109_An_overview_of_the_HYSPLIT_4_modelling_system_for_trajectories/links/004635374253416d4e000000/An-overview-of-the-HYSPLIT-4-modelling-system-for-trajectories.pdf, 1998.

Eastman, R., McCoy, I. L., and Wood, R.: Wind, rain, and the closed to open cell transition in subtropical marine stratocumulus, Journal of Geophysical Research: Atmospheres, 127, e2022JD036 795, https://doi.org/10.1029/2022JD036795, 2022.

https://doi.org/10.5194/egusphere-2025-3776
Preprint. Discussion started: 15 August 2025

Edson, J. B., Jampana, V., Weller, R. A., Bigorre, S. P., Plueddemann, A. J., Fairall, C. W., Miller, S. D., Mahrt, L., Vickers, D., and Hersbach, H.: On the exchange of momentum over the open ocean, Journal of Physical Oceanography, 43, 1589–1610, https://doi.org/10.1175/JPO-D-12-0173.1, 2013.

Fairall, C. W., Bradley, E. F., Rogers, D. P., Edson, J. B., and Young, G. S.: Bulk parameterization of air-sea fluxes for Tropical Ocean-Global Atmosphere Coupled-Ocean Atmosphere Response Experiment, Journal of Geophysical Research: Oceans, 101, 3747–3764, https://doi.org/10.1029/95JC03205, 1996.

Frolicher, T. L., Sarmiento, J. L., Paynter, D. J., Dunne, J. P., Krasting, J. P., and Winton, M.: Dominance of the Southern Ocean in anthropogenic carbon and heat uptake in CMIP5 models, Journal of Climate, 28, 862–886, https://doi.org/10.1175/JCLI-D-14-00117.1, 2015.

Hartigan, J. A. and Wong, M. A.: Algorithm AS 136: A k-means clustering algorithm, Journal of the Royal Statistical Society. Series C (Applied Statistics), 28, 100–108, https://doi.org/10.2307/2346830, 1979.

Hill, K., Moltmann, T., Proctor, R., and Allen, S.: The Australian Integrated Marine Observing System: delivering data streams to address national and international research priorities, Marine Technology Society Journal, 44, 65–72, https://doi.org/10.4031/MTSJ.44.6.13, 2010.

Hoskins, B. J. and Hodges, K. I.: The annual cycle of Northern Hemisphere storm tracks. Part I: Seasons, Journal of Climate, 32, 1743–1760, https://doi.org/10.1175/JCLI-D-17-0870.1, 2019.

Hyder, P., Edwards, J. M., Allan, R. P., Hewitt, H. T., Bracegirdle, T. J., Gregory, J. M., Wood, R., Meijers, A. J. S., Mulcahy, J. P., Field, P. R., et al.: Critical Southern Ocean climate model biases traced to atmospheric model cloud errors, Nature Communications, 9, 3625, https://doi.org/10.1038/s41467-018-05634-2, 2018.

Jeong, H., Park, H.-S., Kang, S. M., and Chung, E.-S.: The greater role of Southern Ocean warming compared to Arctic Ocean warming in shifting future tropical rainfall patterns, Nature Communications, 16, 2790, https://doi.org/10.1038/s41467-025-57654-4, 2025.

Josey, S. A., Grist, J. P., Mecking, J. V., Moat, B. I., and Schulz, E.: A clearer view of Southern Ocean air–sea interaction using surface heat flux asymmetry, Philosophical Transactions of the Royal Society A: Mathematical, Physical and Engineering Sciences, 381, 20220067, https://doi.org/10.1098/rsta.2022.0067, 2023.

Kolstad, E. W. and Bracegirdle, T. J.: Marine cold-air outbreaks in the future: an assessment of IPCC AR4 model results for the Northern Hemisphere, Climate Dynamics, 30, 871–885, https://doi.org/10.1007/s00382-007-0331-0, 2008.

Kuwano-Yoshida, A. and Minobe, S.: Storm-track response to SST fronts in the northwestern Pacific region in an AGCM, Journal of Climate, 30, 1081–1102, https://doi.org/10.1175/JCLI-D-16-0331.1, 2017.

Lang, F., Huang, Y., Siems, S. T., and Manton, M. J.: Characteristics of the marine atmospheric boundary layer over the Southern Ocean in response to the synoptic forcing, Journal of Geophysical Research: Atmospheres, 123, 7799–7820, https://doi.org/10.1029/2018JD028700, 2018.

Lang, F., Ackermann, L., Huang, Y., Truong, S. C., Siems, S. T., and Manton, M. J.: A climatology of open and closed mesoscale cellular convection over the Southern Ocean derived from Himawari-8 observations, Atmospheric Chemistry and Physics, 22, 2135–2152, https://doi.org/10.5194/acp-22-2135-2022, 2022.

Lang, F., Siems, S. T., Huang, Y., Alinejadtabrizi, T., and Ackermann, L.: On the relationship between mesoscale cellular convection and meteorological forcing: comparing the Southern Ocean against the North Pacific, Atmospheric Chemistry and Physics, 24, 1451–1466, https://doi.org/10.5194/acp-24-1451-2024, 2024.

Liu, J., Xiao, T., and Chen, L.: Intercomparisons of air–sea heat fluxes over the Southern Ocean, Journal of Climate, 24, 1198–1211, https://doi.org/10.1175/2010JCLI3699.1, 2011.

https://doi.org/10.5194/egusphere-2025-3776
Preprint. Discussion started: 15 August 2025

Manton, M., Huang, Y., and Siems, S.: Variations in precipitation across the Southern Ocean, Journal of Climate, 33, 10 653–10 670, https://doi.org/10.1175/JCLI-D-20-0120.1, 2020.

McCoy, I. L., Wood, R., and Fletcher, J. K.: Identifying meteorological controls on open and closed mesoscale cellular convection associated with marine cold air outbreaks, Journal of Geophysical Research: Atmospheres, 122, 11 678–11 702, https://doi.org/10.1002/2017JD027031, 2017.

McFarquhar, G., Bretherton, C., Marchand, R., Protat, A., DeMott, P., Alexander, S., Roberts, G., Twohy, C., Toohey, D., Siems, S., and Others: Observations of clouds, aerosols, precipitation, and surface radiation over the Southern Ocean: An overview of CAPRICORN, MARCUS, MICRE, and SOCRATES, Bulletin of the American Meteorological Society, 102, E894–E928, https://doi.org/10.1175/BAMS-D-20-0132.1, 2021.

Meijers, A. J. S.: The Southern Ocean in the Coupled Model Intercomparison Project phase 5, Philosophical Transactions of the Royal Society A: Mathematical, Physical and Engineering Sciences, 372, 20130 296, https://doi.org/10.1098/rsta.2013.0296, 2014.

Monin, A. S. and Obukhov, A. M.: Basic laws of turbulent mixing in the surface layer of the atmosphere, Contrib. Geophys. Inst. Acad. Sci. USSR, 151, 187, available at https://moodle2.units.it/pluginfile.php/507310/mod_resource/content/1/Lezione-giaiotti_081.pdf, 1954.

Montoya Duque, E., Huang, Y., May, P., and Siems, S.: An evaluation of IMERG and ERA5 quantitative precipitation estimates over the Southern Ocean using shipborne observations, Journal of Applied Meteorology and Climatology, 62, 1479–1495, https://doi.org/10.1175/JAMC-D-23-0039.1, 2023.

Naud, C. M., Booth, J. F., and Del Genio, A. D.: The relationship between boundary layer stability and cloud cover in the post-cold-frontal region, Journal of Climate, 29, 8129–8149, https://doi.org/10.1175/JCLI-D-15-0700.1, 2016.

Neiman, P. J., Shapiro, M. A., Donall, E. G., and Kreitzberg, C. W.: Diabatic modification of an extratropical marine cyclone warm sector by cold underlying water, Monthly Weather Review, 118, 1576–1590, https://doi.org/10.1175/1520-0493(1990)118<1576:DMOAEM>2.0.CO;2, 1990.

Risbey, J. S., Pook, M. J., McIntosh, P. C., Wheeler, M. C., and Hendon, H. H.: On the remote drivers of rainfall variability in Australia, Monthly Weather Review, 137, 3233–3253, https://doi.org/10.1175/2009MWR2861.1, 2009.

Sallée, J.-B., Shuckburgh, E., Bruneau, N., Meijers, A., Bracegirdle, T., Wang, Z., and Roy, T.: Assessment of Southern Ocean water mass circulation and characteristics in CMIP5 models: Historical bias and forcing response, Journal of Geophysical Research: Oceans, 118, 1830–1844, https://doi.org/10.1002/jgrc.20135, 2013.

Sandu, I. and Stevens, B.: On the factors modulating the stratocumulus to cumulus transitions, Journal of the Atmospheric Sciences, 68, 1865–1881, https://doi.org/10.1175/2011JAS3614.1, 2011.

Schuddeboom, A. and McDonald, A.: The Southern Ocean radiative bias, cloud compensating errors, and equilibrium climate sensitivity in CMIP6 models, Journal of Geophysical Research: Atmospheres, 126, e2021JD035 310, https://doi.org/10.1029/2021JD035310, 2021.

Schulz, E., Josey, S. A., and Verein, R.: First air-sea flux mooring measurements in the Southern Ocean, Geophysical Research Letters, 39, https://doi.org/10.1029/2012GL052290, 2012.

Shaman, J., Samelson, R. M., and Skyllingstad, E.: Air–sea fluxes over the Gulf Stream region: Atmospheric controls and trends, Journal of Climate, 23, 2651–2670, https://doi.org/10.1175/2010JCLI3269.1, 2010.

Siems, S. T., Huang, Y., and Manton, M. J.: Southern Ocean precipitation: Toward a process-level understanding, Wiley Interdisciplinary Reviews: Climate Change, 13, e800, https://doi.org/10.1002/wcc.800, 2022.

Small, R. J. d., deSzoeke, S. P., Xie, S.-P., O'Neill, L., Seo, H., Song, Q., Cornillon, P., Spall, M., and Minobe, S.: Air–sea interaction over ocean fronts and eddies, Dynamics of Atmospheres and Oceans, 45, 274–319, https://doi.org/10.1016/j.dynatmoce.2008.01.001, 2008.

https://doi.org/10.5194/egusphere-2025-3776
Preprint. Discussion started: 15 August 2025

Su, Z., Wang, J., Klein, P., Thompson, A. F., and Menemenlis, D.: Ocean submesoscales as a key component of the global heat budget, Nature Communications, 9, 775, https://doi.org/10.1038/s41467-018-02983-w, 2018.

Swart, S., Gille, S. T., Delille, B., Josey, S. A., Mazloff, M. R., Newman, L., Thompson, A. F., Thomson, J., Ward, B., Du Plessis, M. D., et al.: Constraining Southern Ocean air-sea-ice fluxes through enhanced observations, Frontiers in Marine Science, 6, 421, https://doi.org/10.3389/fmars.2019.00421, 2019.

Truong, S. C. H., Huang, Y., Lang, F., Messmer, M., Simmonds, I., Siems, S. T., and Manton, M. J.: A climatology of the marine atmospheric boundary layer over the Southern Ocean from four field campaigns during 2016–2018, Journal of Geophysical Research: Atmospheres, 125, e2020JD033 214, https://doi.org/10.1029/2020JD033214, 2020.

Valdivieso, M., Haines, K., Balmaseda, M., Chang, Y.-S., Drevillon, M., Ferry, N., Fujii, Y., Köhl, A., Storto, A., Toyoda, T., et al.: An assessment of air–sea heat fluxes from ocean and coupled reanalyses, Climate Dynamics, 49, 983–1008, https://doi.org/10.1007/s00382-015-2843-3, 2017.

Williams, R. G., Meijers, A. J. S., Roussenov, V. M., Katavouta, A., Ceppi, P., Rosser, J. P., and Salvi, P.: Asymmetries in the Southern Ocean contribution to global heat and carbon uptake, Nature Climate Change, 14, 823–831, https://doi.org/10.1038/s41558-024-02066-3, 2024.

Wood, R. and Hartmann, D. L.: Spatial variability of liquid water path in marine low cloud: The importance of mesoscale cellular convection, Journal of Climate, 19, 1748–1764, https://doi.org/10.1175/JCLI3702.1, 2006.

Wyant, M. C., Bretherton, C. S., Rand, H. A., and Stevens, D. E.: Numerical simulations and a conceptual model of the stratocumulus to trade cumulus transition, Journal of the Atmospheric Sciences, 54, 168–192, https://doi.org/10.1175/1520-0469(1997)054<0168:NSAACM>2.0.CO;2, 1997.

Yau, M. K. and Jean, M.: Synoptic aspects and physical processes in the rapidly intensifying cyclone of 6–8 March 1986, Atmosphere-Ocean, 27, 59–86, https://doi.org/10.1080/07055900.1989.9649328, 1989.

Yokoyama, Y. and Yamamoto, M.: Influences of surface heat flux on twin cyclone structure during their explosive development over the East Asian marginal seas on 23 January 2008, Weather and Climate Extremes, 23, 100 198, https://doi.org/10.1016/j.wace.2019.100198, 2019.

https://doi.org/10.5194/egusphere-2025-3776
Preprint. Discussion started: 15 August 2025

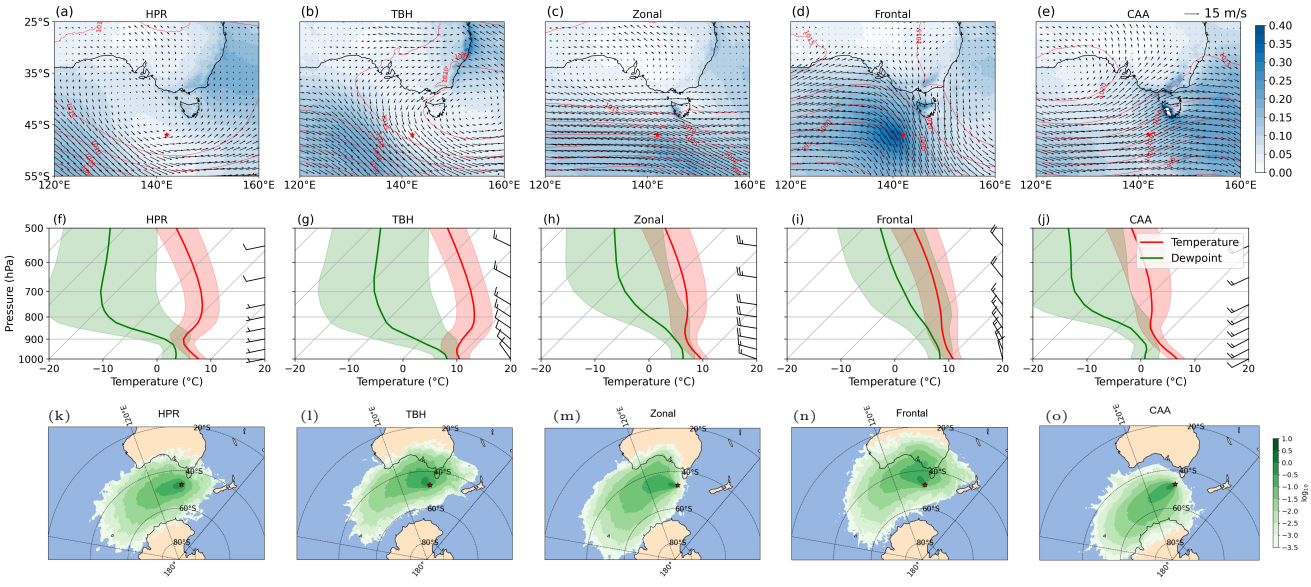

Figure 1. Characteristics of synoptic regimes: (a-e) Spatial distributions of rainfall (shaded, unit: mm/hr), mean sea-level pressure (MSLP, contours, unit: hPa) and wind (vector, unit: m/s) at 975 hPa over the SO for five major synoptic types during 1990–2023. The red mark in the figure represents the location, 47°S and 142°E, where the IMOS buoy is deployed. (f-h) Composite of Skewt-Logp thermodynamic diagram for synoptic types over the SO. Red and blue lines represent mean profiles of temperature and dew point temperature, respectively, and the shaded region indicates their standard deviation. Wind barbs on the right of the figure indicate the speed and direction of wind at different pressure levels. (k-m) 72-hour back trajectories of air parcels at 1000 m altitude for the synoptic regimes at SOFS.

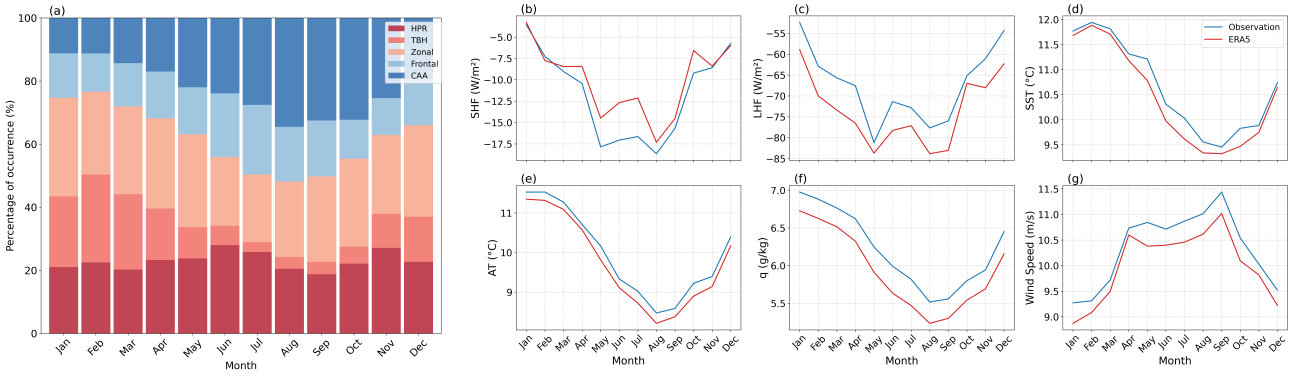

Figure 2. Seasonality: (a) Seasonality of synoptic regimes at the SOFS. (b-g) Seasonality of SHF and LHF and their drivers at SOFS.

https://doi.org/10.5194/egusphere-2025-3776
Preprint. Discussion started: 15 August 2025

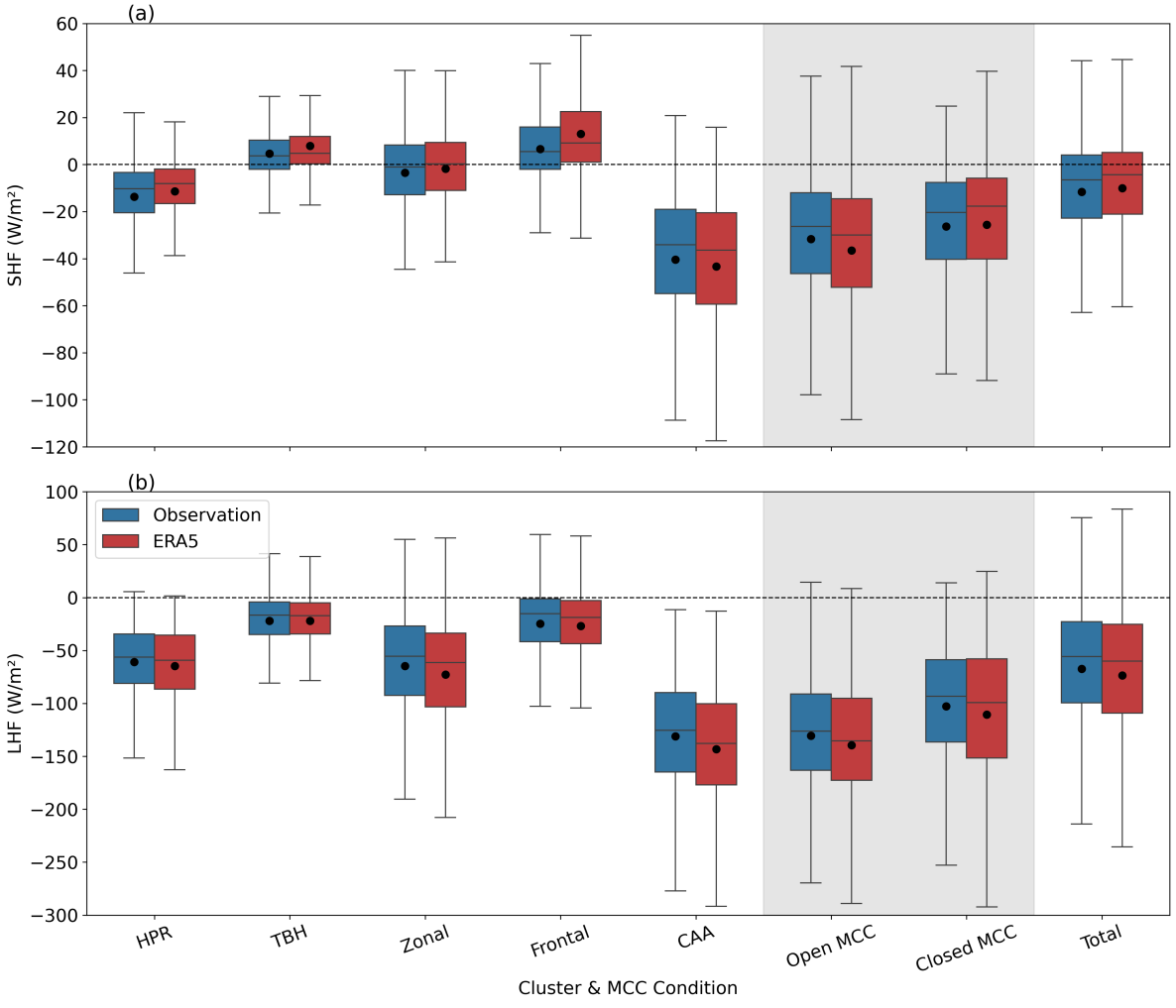

Figure 3. Synoptic regimes and air-sea interaction: Box plots for the buoy and ERA5 derived SHF and LHF corresponding to different synoptic types and open/closed MCC at SOFS. The horizontal line within the box represents the median (50th percentile), and the black dots represent the mean of the distribution.

https://doi.org/10.5194/egusphere-2025-3776
Preprint. Discussion started: 15 August 2025

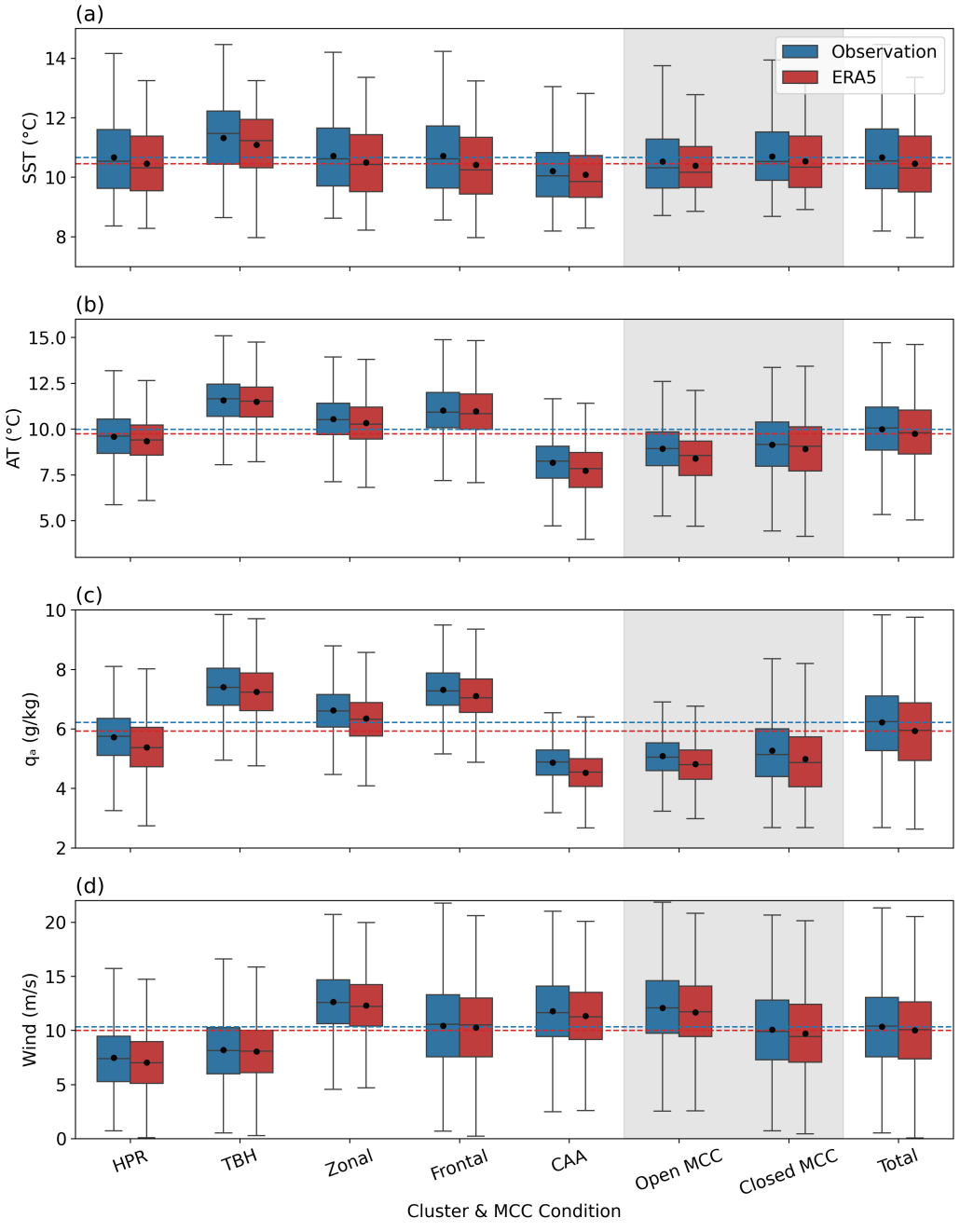

Figure 4. Influence of synoptic regimes on surface meteorology: Box plots of buoy and ERA5 derived SST, AT, qa and wind speed for synoptic types and open/closed MCC at SOFS. The horizontal line within the box represents the median (50th percentile), and the black dots represent the mean of the distribution. The red and blue horizontal dotted lines represent the overall means of each variable from ERA5 and buoy, respectively.

https://doi.org/10.5194/egusphere-2025-3776
Preprint. Discussion started: 15 August 2025

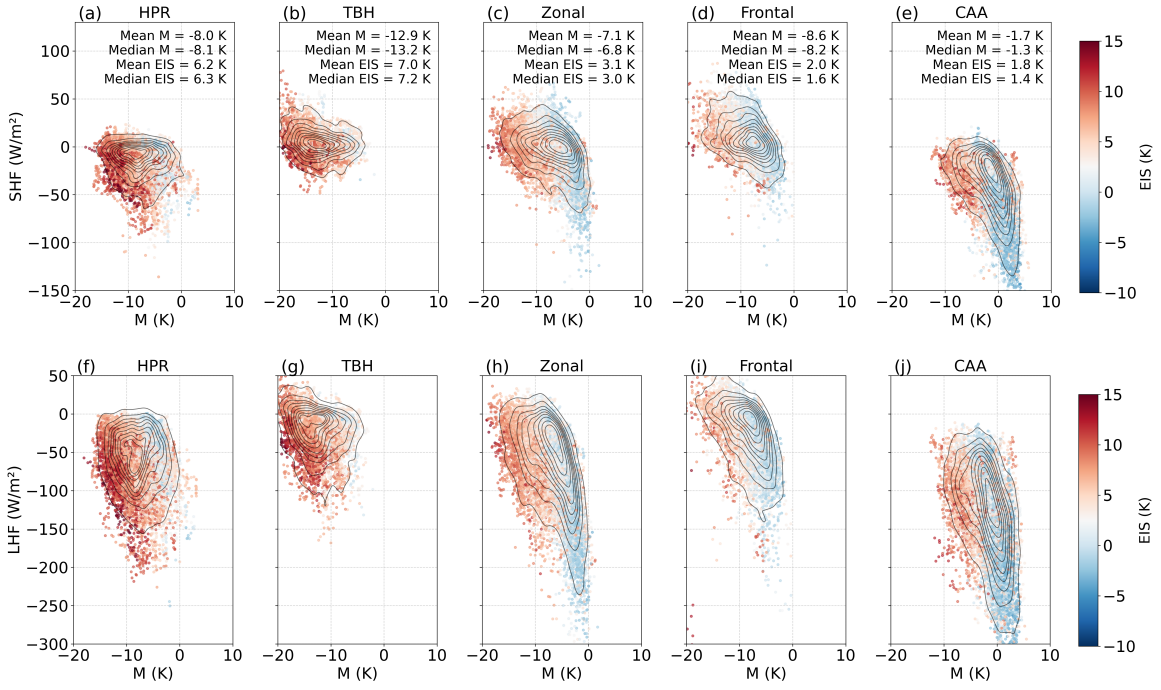

Figure 5. Influence of synoptic regimes on atmospheric stability and inversion strength: Two-dimensional density distribution of M-index vs SHF and LHF for synoptic regimes at SOFS. EIS is overlaid as a colour scale, illustrating their variation with the distribution.

https://doi.org/10.5194/egusphere-2025-3776
Preprint. Discussion started: 15 August 2025

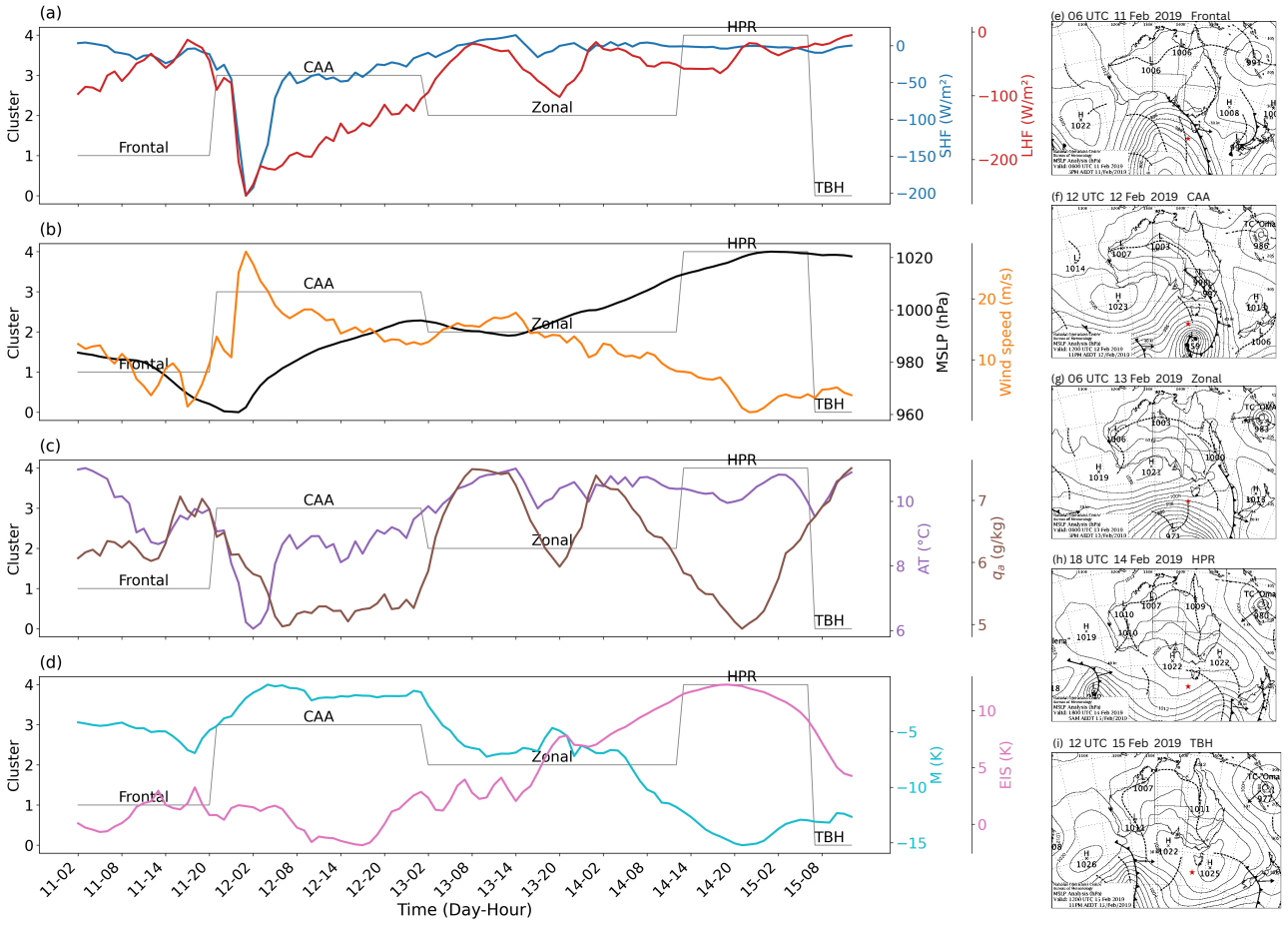

Figure 6. Case study: Time series of (a) SHF and LHF, (b) MSLP and wind speed, (c) AT and qa, (d) M-index and EIS during the transition from one cluster (synoptic regime) to another. (e-i) Spatial distribution of MSLP for synoptic regimes (source: Bureau of Meteorology). The red star indicates the location of the IMOS buoy.

https://doi.org/10.5194/egusphere-2025-3776
Preprint. Discussion started: 15 August 2025

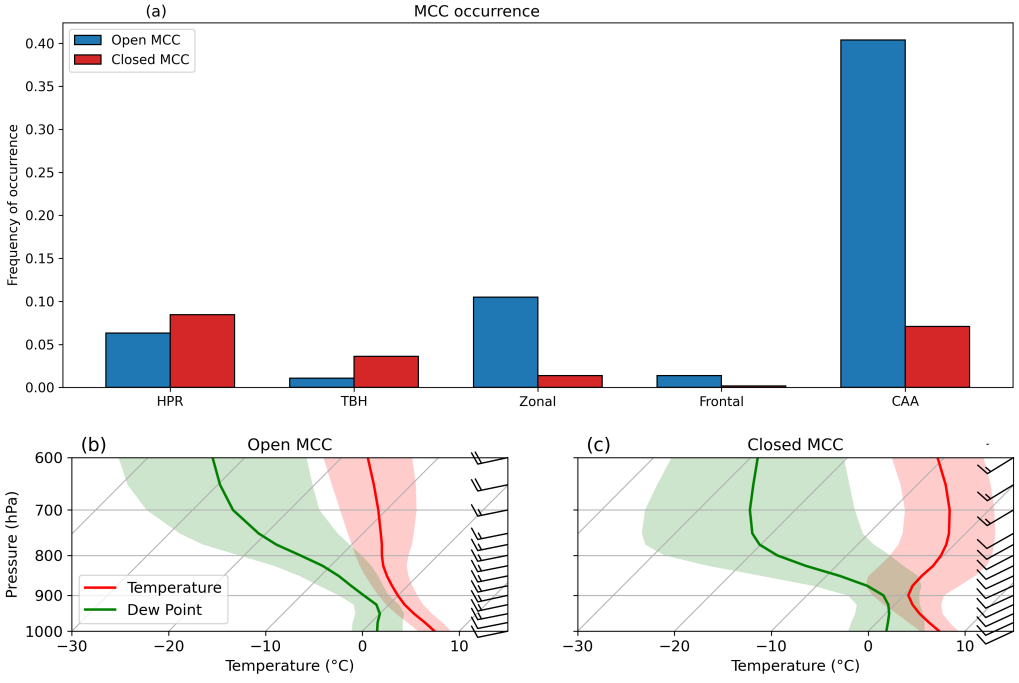

Figure 7. Influence of synoptic regimes on open and closed MCC: (a) The frequency of open and closed MCC occurrence is associated with synoptic types. (b, c) The composite of the Skewt-Logp thermodynamic diagram for open and closed MCC conditions.

https://doi.org/10.5194/egusphere-2025-3776
Preprint. Discussion started: 15 August 2025

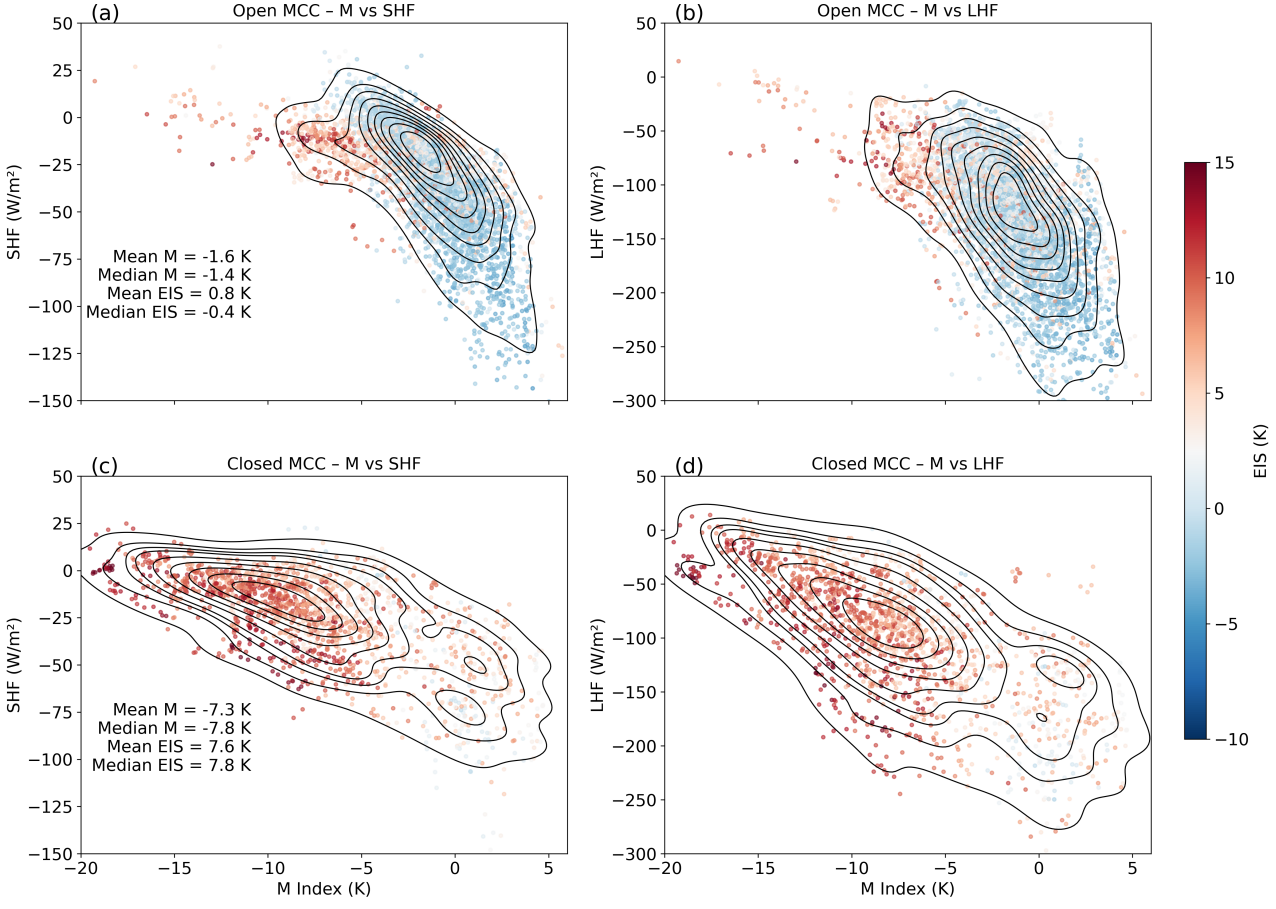

Figure 8. Atmospheric stability and inversion strength for open and closed MCC: The two-dimensional density distribution of M-index vs SHF and LHF for open and closed MCC. EIS is overlaid as a colour scale, illustrating their variation with the distribution.

https://doi.org/10.5194/egusphere-2025-3776
Preprint. Discussion started: 15 August 2025

Cluster	SHF (Obs)		LHF (Obs)		SHF (ERA5)		LHF (ERA5)	
	Mean	Median	Mean	Median	Mean	Median	Mean	Median
HPR	-13.64	-10.30	-60.77	-56.27	-11.40	-8.06	-64.63	-59.30
TBH	4.64	3.68	-21.90	-16.72	7.95	4.76	-21.95	-17.03
Zonal	-3.45	-1.10	-64.63	-55.46	-1.83	0.26	-72.83	-61.30
Frontal	6.62	5.45	-24.75	-15.29	13.01	9.15	-26.98	-18.77
CAA	-40.38	-34.10	-131.12	-125.44	-43.32	-36.40	-143.22	-137.71
Open MCC	-31.65	-26.31	-130.55	-126.10	-36.51	-29.94	-139.47	-135.41
Closed MCC	-26.37	-20.39	-102.85	-93.38	-25.61	-17.70	-110.59	-99.22
Total	**-11.65**	**-6.57**	**-67.46**	**-55.82**	**-9.99**	**-4.28**	**-73.62**	**-59.94**

Table 1. Comparison of SHF and LHF mean and median values (unit: W/m^2) from buoy observations and ERA5 across different clusters.

Cluster	SHF RMSE	SHF Bias	SHF Corr	LHF RMSE	LHF Bias	LHF Corr
HPR	9.64	2.24	0.79	19.75	-3.86	0.87
TBH	9.16	3.31	0.81	16.05	-0.05	0.81
Zonal	12.77	1.63	0.80	27.12	-8.20	0.87
Frontal	13.71	6.40	0.79	22.96	-2.23	0.80
CAA	15.14	-2.93	0.88	31.46	-12.11	0.87
Open MCC	14.68	-4.86	0.89	28.95	-8.92	0.88
Closed MCC	10.97	0.76	0.92	24.02	-7.74	0.94
Total	**12.47**	**1.66**	**0.90**	**24.94**	**-6.16**	**0.92**

Table 2. Root mean square error (RMSE, unit:W/m^2), bias (unit: W/m^2), and correlation of SHF and LHF from ERA5 compared to buoy observations across different clusters.